

CrossMark  
click for updatesCite this: *J. Mater. Chem. A*, 2015, 3, 6853

# Analysis and characterization of iron pyrite nanocrystals and nanocrystalline thin films derived from bromide anion synthesis†

Khagendra P. Bhandari,<sup>\*a</sup> Paul J. Roland,<sup>a</sup> Tyler Kinner,<sup>a</sup> Yifang Cao,<sup>a</sup> Hyekyoung Choi,<sup>b</sup> Sohee Jeong<sup>bc</sup> and Randy J. Ellingson<sup>\*a</sup>

We use a solution-based hot injection method to synthesize stable, phase pure and highly crystalline cubic iron pyrite (FeS<sub>2</sub>) nanocrystals, with size varying from ~70 to 150 nm. We use iron(II) bromide as an iron precursor, elemental sulfur as the sulfur source, trioctylphosphine oxide (TOPO) and 1,2-hexanediol as capping ligands, and oleylamine (OLA) as a non-coordinating solvent during the synthesis. We report on the influence of hydrazine treatment, and of thermal sintering, on the morphological, electronic, optical, and surface chemical properties of FeS<sub>2</sub> films. Four point probe and Hall measurements indicate that these iron pyrite films are highly conductive. Although they are unsuitable as an effective photovoltaic light-absorbing layer, they offer clear potential as a conducting contact layer in photovoltaic and other optoelectronic devices.

Received 19th November 2014  
Accepted 12th February 2015

DOI: 10.1039/c4ta06320a

www.rsc.org/MaterialsA

## 1. Introduction

Iron pyrite (FeS<sub>2</sub>) has attracted considerable attention as a potential absorption layer in thin film photovoltaics (PV) because of its abundance, low toxicity, high absorption coefficient in the near-infrared and visible spectral regions,<sup>1–3</sup> suitable band gap energy,<sup>4,5</sup> and low material cost.<sup>6–8</sup> Although the ~0.95 eV bandgap energy of bulk FeS<sub>2</sub> corresponds to a thermodynamically attainable photo-conversion efficiency of >20%,<sup>9</sup> the record device efficiency stands at just ~2.8% as achieved by the Tributsch group in the 1980s.<sup>6</sup> In recent years, FeS<sub>2</sub> nanocrystals (NCs) have been investigated as a potential route to efficient solution-based PV technologies.<sup>7,10–15</sup> Despite considerable additional effort, no improvement in FeS<sub>2</sub>-absorber-based PV performance has yet been demonstrated.

Previous thermal injection syntheses of colloidal iron pyrite NCs have utilized chlorine-halogenated iron precursors such as

FeCl<sub>2</sub>·4H<sub>2</sub>O, FeCl<sub>2</sub> and FeCl<sub>3</sub>.<sup>7,8,10,16–19</sup> Similarly, iron pyrite NCs have been prepared *via* hydrothermal synthesis using a single source precursor which is initially prepared using iron(III) chloride (FeCl<sub>3</sub>).<sup>2,20–22</sup> In this paper, we report on the use of iron(II) bromide (FeBr<sub>2</sub>) as a new iron precursor for FeS<sub>2</sub> NC synthesis in the hot solution injection process. Anhydrous FeBr<sub>2</sub> has already been used in a number of syntheses of iron compounds due to its relatively high solubility in organic solvents,<sup>23,24</sup> though to our knowledge, no previous report has been made on the synthesis of iron pyrite employing FeBr<sub>2</sub> as a precursor. Iron pyrite is an Earth-abundant and non-toxic material and, based on the globally harmonized system of classification and labeling of chemicals (GHS), using iron(II) bromide rather than iron(II) chloride reduces the toxicity of the synthetic route to FeS<sub>2</sub> NCs. Iron compounds halogenated with chlorine are corrosive, and represent acute and chronic hazards to human and aquatic environments; in contrast, FeBr<sub>2</sub> does not possess any of these labels.<sup>25</sup> In addition, iron(II) chloride exhibits greater sensitivity to air and moisture, whereas sensitivity of FeBr<sub>2</sub> to air and moisture is negligible. Moreover, we find that the use of FeBr<sub>2</sub>, together with carefully-optimized thermal treatment stages, facilitates the reproducible preparation of highly crystalline, phase pure and air stable FeS<sub>2</sub> NCs; we report here on the characterization of these pyrite NCs in solution and thin film form.

Sheet resistance, resistivity, majority carrier type, carrier density, and mobility of thin films are important properties of semiconductors and are critical parameters in materials research. These physical parameters explain the transport behaviors of semiconductor films which determine their potential utility for device applications. Significant studies of

<sup>a</sup>Department of Physics and Astronomy, The University of Toledo, 2801 W. Bancroft Street, Toledo, OH 43606, USA. E-mail: randy.ellingson@utoledo.edu; Tel: +1-419-530-3874

<sup>b</sup>Department of Nanomechatronics, Korea University of Science and Technology, Daejeon 305-350, South Korea

<sup>c</sup>Nanomechanical Research Division, Korea Institute of Machinery and Materials, Daejeon 305-343, South Korea

† Electronic supplementary information (ESI) available: Band gap calculation for FeS<sub>2</sub> NC film, absorbance before and after hydrazine treatment, TEM image and size distribution of NCs, characterizations of oleylamine and 1,2-hexanediol capped NCs, SEM images before and after sintering, grain size calculation based on Scherrer analysis, electrical four point probe measurements and work function calculation of FeS<sub>2</sub> before and after hydrazine treatment. See DOI: 10.1039/c4ta06320a

these properties for iron pyrite NC films remain relatively rare,<sup>7</sup> although some reports exist for iron pyrite films prepared by spray pyrolysis, electrodeposition, sol-gel and molecular ink methods respectively.<sup>26–29</sup> In this work, we employ hot probe, four point probe, and Hall measurement to characterize the electronic properties of FeS<sub>2</sub> NC-based films, and to assess their applicability within electronic devices.

## 2. Experimental

### 2.1 Synthesis of FeS<sub>2</sub> NCs

The FeS<sub>2</sub> NCs were synthesized by injection of sulfur into decomposed metal precursor followed by nucleation and growth. All syntheses were done under nitrogen atmosphere using standard Schlenk line techniques. In a typical synthesis, about 1.49 mmol of FeBr<sub>2</sub> (~321 mg) and 3 mmol (~1.16 g) of trioctylphosphine oxide (TOPO) or 3.2 mmol (~0.4 mL) of 1,2-hexanediol are mixed in 30 mL of oleylamine (OLA) in a three neck flask under constant stirring. The FeBr<sub>2</sub> mixture is heated to 170 °C for ~2 hours and 30 minutes using a heating mantle; during this time, the sulfur precursor solution is prepared. For this, 8.98 mmol of elemental sulfur (~288 mg) is dissolved at room temperature in 15 mL of OLA; for complete dissolution of sulfur in OLA, ~10 minutes of ultra-sonication is performed. The sulfur solution is kept in hot water bath at ~90 °C. After 2 hours and 30 minutes, the temperature of the FeBr<sub>2</sub> solution is raised toward 220 °C, and once it exceeds 216 °C, the sulfur solution is rapidly injected. Nucleation of FeS<sub>2</sub> clusters initiates upon sulfur injection, and the growth of FeS<sub>2</sub> NCs proceeds at a temperature of 220 °C.

Following two hours at 220 °C, the NC solution is allowed to cool to room temperature, with continued stirring, in an N<sub>2</sub> atmosphere. Nanocrystals so obtained are washed a minimum of three times using methanol as a non-solvent and toluene or chloroform as solvent. For the first wash, methanol is added to the as-synthesized NC solution, followed by centrifugation for 10 minutes at ~2400 × *g*. After decanting the supernatant, NCs were dispersed in toluene or chloroform with the assistance of sonication, and methanol is added to precipitate the NCs allowing for physical separation *via* centrifugation. The wash procedure is repeated one more time, and then the NCs are dried under nitrogen gas flow.

In the synthesis process, TOPO may be used as the surfactant and OLA as a non-coordinating solvent; in this method, FeS<sub>2</sub> NCs so obtained are understood to be capped by TOPO. We have found that high quality FeS<sub>2</sub> NCs can alternatively be synthesized using OLA without the presence of TOPO. Likewise, high-quality FeS<sub>2</sub> NCs can be synthesized using 1,2-hexanediol as the surfactant and OLA as a non-coordinating solvent.

### 2.2 FeS<sub>2</sub> film fabrication

Because of their large size (~70–150 nm), FeS<sub>2</sub> NCs do not remain in stable suspension for long periods of time and a well-dispersed but unstirred solution will effectively change in concentration as the NCs settle to the bottom of the container. Therefore, we are unable to readily use a dip-coating method to

make NC films and we instead formed films *via* drop-casting in a layer-by-layer (LbL) manner.<sup>30,31</sup> To fabricate the FeS<sub>2</sub> NC films, we prepare the FeS<sub>2</sub> NC solution in chloroform at a concentration of ~6 mg mL<sup>-1</sup> and proceed with film formation in an N<sub>2</sub> environment. A layer of drop-cast NCs is deposited onto the chosen substrate, and allowed to dry. At this point, the film can optionally be treated with hydrazine for ligand removal (*vide infra*). In the case of an untreated film, the film thickness may be increased by simply repeating the drop-cast process followed by the drying process; preparation of a 1 μm film typically requires 2 cycles.

To prepare more highly conductive NC films, long chain hydrocarbon molecules (C<sub>24</sub>H<sub>51</sub>OP, TOPO) were removed from the NC surface in the LbL process by cyclically treating films with 1 M hydrazine in ethanol. We prepared these surfactant-free FeS<sub>2</sub> films as follows. Subsequent to the first FeS<sub>2</sub> NC drop-cast layer deposition, the film is allowed to dry in the N<sub>2</sub> environment. The film is subsequently submerged in a 1 M hydrazine solution in ethanol for ~2 minutes. The film is withdrawn from the hydrazine solution and immediately submerged into a pure ethanol solution to remove any residual surfactant or hydrazine – *i.e.*, as a rinse. The film is then allowed to dry. Repeating the drop-cast/dry/hydrazine/rinse/dry process multiple times allows for preparation of films of the desired thickness.

FeS<sub>2</sub> NC films prepared by the LbL drop-casting method exhibit microscopic areas of incomplete coverage by FeS<sub>2</sub> (*i.e.*, pinholes) which persist even up to 1 μm film thickness. In addition, one typically observes improved charge transport in semiconductor NC or quantum dots films once neighboring NCs are brought into improved contact through removal of surfactant molecules. In an effort to ameliorate the presence of pinholes, and to investigate possible control over electronic properties, we sintered FeS<sub>2</sub> NC films; sintering is carried out in the presence of sulfur vapor to reduce the likelihood of sulfur dissociation from the Fe–S bond in FeS<sub>2</sub>. Sintering may anneal the NCs together and/or promote grain growth, resulting in a film exhibiting more uniform coverage and/or improved electronic properties. Sintering of the films is conducted in a cylindrical quartz tube furnace such that the film is heated radially. In the quartz tube, two heaters are arranged: one for evaporating elemental sulfur at ~350 °C and the other for heating the sample and substrate for annealing. The ends of the quartz tube are capped with flanges incorporating small diameter gas flow tubes. Initially the sample tube is purged with a forming gas (95% argon, 5% hydrogen) for ~6 minutes, and then low pressure argon gas (5 sccm) is introduced during the sintering process. The sintering process proceeds with the substrate and film held at a temperature of 500 °C or 540 °C, within a sulfur vapor, for 1–3 hours.

## 3. Results and discussion

Fig. 1 shows the optical absorption for NC FeS<sub>2</sub> both in chloroform solution as well as in thin-film form as deposited onto uncoated soda lime glass. Light absorption is strong for wavelengths below ~1 μm; beyond about 1.2 μm, the film is more,

but incompletely, transmissive. The absorption of light in the infrared region below the indirect band gap energy (0.95 eV, 1305 nm) has been ascribed to S vacancies in the FeS<sub>2</sub> film.<sup>32</sup> However, Yu *et al.* recently reported that FeS<sub>2</sub> NC films, which show p-type defects and a high free carrier concentration, are prone to the formation of low-energy phases of Fe:S stoichiometry exceeding 0.5;<sup>3</sup> such phases include troilite (FeS) and pyrrhotite (FeS<sub>1+x</sub>,  $x = 0 - 1/7$ ). Thus, the sub-bandgap infrared absorption may be due to absorption caused by non-FeS<sub>2</sub> iron sulfide phases. We have estimated the direct and indirect band gaps of FeS<sub>2</sub> NCs in film *via* absorbance spectroscopy (ESI, Fig. S1†), finding values of  $\sim 1.3$  eV and  $\sim 0.95$  eV respectively.<sup>33,34</sup> These data agree well with literature values reported by Bi *et al.* (1.38 eV and 0.93 eV, respectively).<sup>7</sup> Various other groups have reported band gap energies in the range of 0.82–1.6 eV, with most results for the indirect gap near to 0.9 eV.<sup>35–39</sup> Fig. 1 (red) shows the absorption coefficient of an untreated FeS<sub>2</sub> NC film of thickness  $\sim 150$  nm. The absorption coefficient is very strong,  $\geq 10^5$  cm<sup>-1</sup> in the visible and near-infrared region of the spectrum.

Hydrazine treatment of the films is confirmed by FTIR spectroscopy measurement (Fig. S2a†). The C–H stretch signatures near 3000 cm<sup>-1</sup> and at 1500 cm<sup>-1</sup> show quantitative removal and/or replacement of TOPO (or 1,2-hexanediol) through hydrazine treatment. Absorbance spectra of NC films before and after the hydrazine treatment are shown in Fig. S2b.† The absorbance spectrum shows that hydrazine does not change the material properties of iron pyrite. Hydrazine has been widely used in solution process depositions of thin films, which is considered as a potential low cost route for fabrication of electronic devices. For example, CZTS and CZTSSe based solar cells using a hydrazine-based solution process have reached an energy conversion efficiency exceeding 10%.<sup>40,41</sup>

Characterization of the structural and compositional properties of our FeS<sub>2</sub> thin films shows consistent evidence for high-purity pyrite FeS<sub>2</sub>. X-ray diffraction (XRD) data were collected with a Rigaku Ultima III diffractometer using Cu K $\alpha$  radiation in focused beam geometry. Scanning electron microscopy

(SEM) imaging was conducted at operating voltages of 10 kV and 20 kV. Energy-dispersive X-ray spectroscopy (EDX) measurements, used to quantify film stoichiometry, were conducted at an operating voltage of 20 kV with a working distance of 15 mm. Raman spectroscopy measurements were conducted using a laser beam of wavelength 633 nm. Fig. 2 shows the XRD, Raman scattering, SEM, and EDX data for as-deposited FeS<sub>2</sub> NC films. For XRD, the NC film was prepared on a Si substrate for zero background, whereas for SEM and Raman the films were prepared on soda lime glass. The XRD image in Fig. 2a shows pure FeS<sub>2</sub> cubic phase with no evidence of other crystal structures. The sharp peaks in the XRD pattern indicate excellent crystallinity of the as-synthesized FeS<sub>2</sub> NCs. Fig. 3b shows the Raman spectrum of an as-synthesized drop-cast FeS<sub>2</sub> NC film, measured with 632 nm excitation. Raman peaks at 343.7 cm<sup>-1</sup>, 380 cm<sup>-1</sup> and 431 cm<sup>-1</sup>, corresponding to the A<sub>g</sub>, E<sub>g</sub>, and T<sub>g</sub>(3) vibrational modes, are consistent with phonon vibrations previously observed for FeS<sub>2</sub>.<sup>7,16,42–44</sup> These previously reported Raman results were based on 532 nm excitation of FeS<sub>2</sub> film contrary to 633 nm used in this study. The Raman peaks we observe are well separated from Raman peaks reported for troilite (FeS) which shows peaks at  $\sim 210$  cm<sup>-1</sup> and  $\sim 280$  cm<sup>-1</sup>.<sup>45,46</sup>

Uniform cubically-shaped FeS<sub>2</sub> NCs synthesized with TOPO/OLA combinations are shown in Fig. 2c. The size of the NCs can be varied from  $\sim 70$  nm to  $\sim 150$  nm by varying the surfactant concentration during synthesis. To calculate size distributions of TOPO capped NCs, TEM images (Fig. S3†) were analyzed using *ImageJ* software.<sup>47</sup> The size distribution of the FeS<sub>2</sub> NCs shown in Fig. 2c yielded an average edge length of  $133 \pm 18$  nm. We note also that the nanocrystallites in Fig. S3 and S4† show some variation in the apparent polycrystallinity; *i.e.*, some samples appear to consist of crystallites in which smaller nanocrystals have attached or aggregated to form larger particles.<sup>48</sup>

The  $V_{OC}$  limitation that has been observed in solar cells using FeS<sub>2</sub> as the absorber layer has been ascribed to sulfur deficiency.<sup>49</sup> Significant changes in the crystalline structure and therefore the electronic properties of compound semiconductors can arise from formation of phases that may correspond to relatively small deviations in stoichiometry. After initial successes by Tributsch *et al.*,<sup>6</sup> improvements in the efficiency of FeS<sub>2</sub> solar cells have been elusive. Many authors have found a significant decrease in S : Fe ratio in nominally FeS<sub>2</sub> samples, ranging from 2 : 1 to 1.74 : 1.<sup>32,50</sup> Iron pyrite NCs synthesized in our laboratory exhibit an essentially stoichiometric ratio. Fig. 2d shows EDX measurement results for seven different batches of FeS<sub>2</sub> NCs, synthesized with varying amounts of surfactant, yielding an average S : Fe ratio of 2.01 : 1. Nonetheless, it merits noting that even small amounts of phase impurities, especially those near the 2 : 1 S : Fe ratio, may noticeably alter the aggregate optical and electronic properties. Detailed characterization of FeS<sub>2</sub> NCs synthesized using OLA and 1,2-hexanediol as surfactants are provided in the ESI.†

The poor performance of the FeS<sub>2</sub> NCs solar cells fabricated in our laboratory is thought to be due in part to the pinholes which yield shunted devices. Pinholes in FeS<sub>2</sub> thin films have

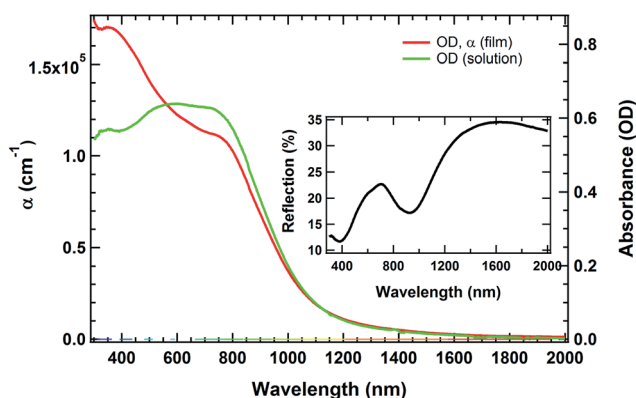


Fig. 1 Absorption spectra for the as-obtained (TOPO capped) NCs dispersed in chloroform (green) and as a drop-cast film on soda lime glass (red). The film's absorption coefficient is also shown, along the left axis. Inset: the as-obtained (untreated) NC film reflectance spectrum showing peaks at  $\sim 700$  nm and 1600 nm.

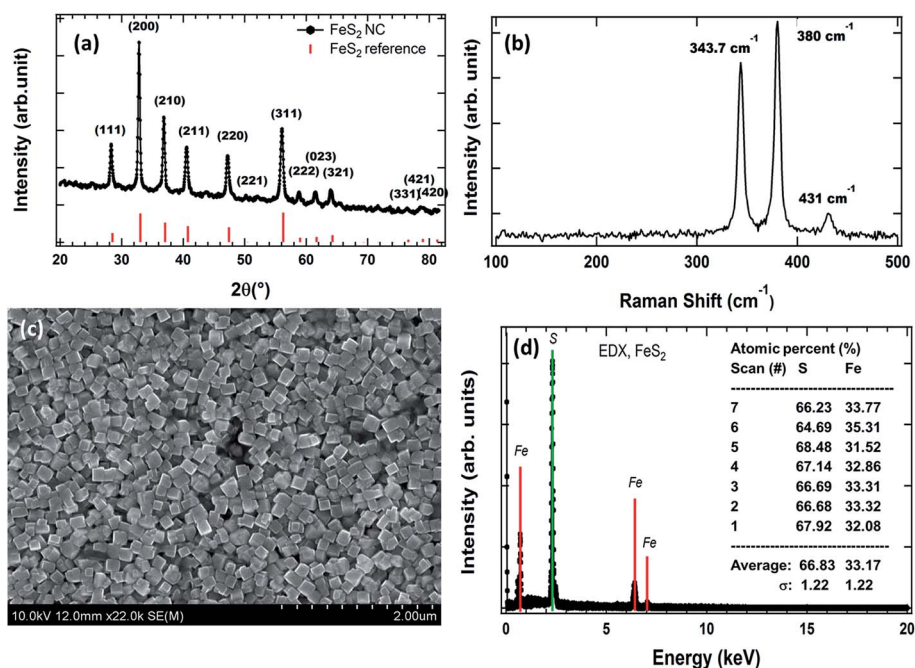


Fig. 2 Characterization of as-deposited, drop-cast  $\text{FeS}_2$  NC films using NCs of size  $\sim 130$  nm. (a) XRD spectrum (focused beam), (b) Raman scattering spectrum, (c) SEM image at 10 kV accelerating potential (d) EDX measurement of seven  $\text{FeS}_2$  NC films prepared from distinct NC syntheses.

been previously noted and addressed; for example, Kment *et al.* used a novel sol-gel route to get pinhole-free  $\text{FeS}_2$  thin films.<sup>51</sup> In addition, Smestad *et al.* described pinholes in their  $\text{FeS}_2$  thin films formed by spray pyrolysis.<sup>52</sup> They attributed pinholes to strain at the substrate-film interface, and to the cooling action of the spray droplets and the differences in thermal expansion between iron pyrite and the glass materials. The authors found fewer pinholes for films sprayed at a lower rate. We have followed a different approach to remove pinholes in  $\text{FeS}_2$  NC thin

films. The hydrazine treated films were sintered at a high temperature. Iron pyrite is thermodynamically unstable when heated above  $\sim 300$  °C for long periods of time; we observe that heating for longer than  $\sim 15$  minutes at  $\sim 400$  °C, or heating at a higher temperature, resulted in conversion of pyrite to troilite ( $\text{FeS}$ ) phase. Under such intense sintering conditions, the NC films were heated in sulfur vapor (in argon) to prevent sulfur evaporation and maintain the S : Fe ratio. Nanocrystal films are

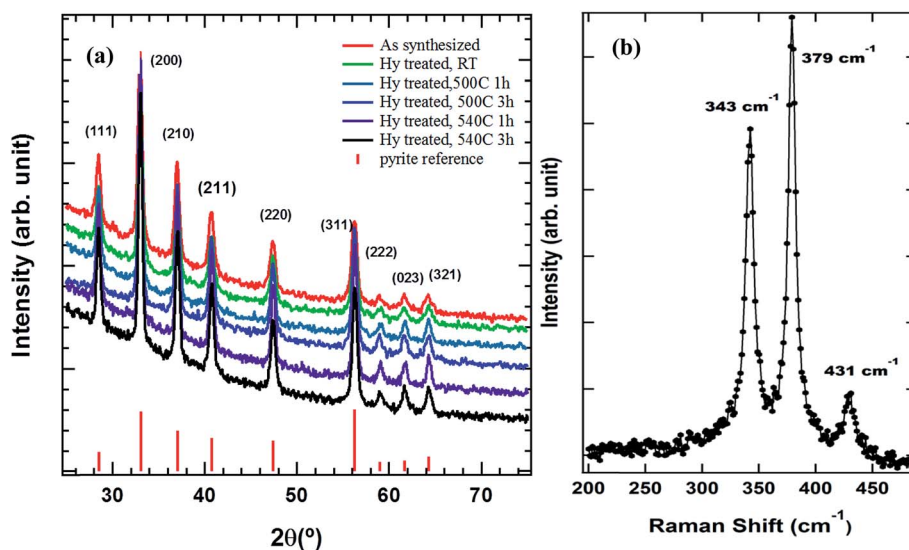


Fig. 3 Characterization of  $\text{FeS}_2$  NC films deposited by LbL drop-cast method using NC of size  $\sim 70$  nm: (a) XRD spectra showing the effect of hydrazine and thermal annealing treatment, (b) Raman spectrum for a film annealed at 540 °C for 1 hour.

sintered at 500 °C and 540 °C from one to three hours in sulfur vapor.

Fig. 3a shows XRD spectra of FeS<sub>2</sub> NC films before and after annealing the films. Raman spectroscopy is more sensitive than conventional XRD to determine the structural purity of the NC films before and after sulfur annealing. Raman spectra in Fig. 3b are sharper and more intense because of the crystallinity of the film after annealing. Puthussery *et al.* sintered FeS<sub>2</sub> films at 540 °C for 4 hours and found significant grain growth.<sup>8</sup> In our case, heating at 540 °C from one to three hours did not yield appreciable observable grain growth of surface NCs on the films (Fig. S5†) but helped to some extent to block the pinholes based on optical microscopic observation. The XRD spectrum in Fig. 3a, however, shows improvement in crystallinity after sintering the film (see Table 1). EDX measurement shows that atomic percentage of S/Fe before and after annealing the film remain same which indicates that the films are thermodynamically stable in sulfurization. Considering the intense (200) peak, full width at half maxima (FWHM) and grain size were calculated for all XRD spectra for samples annealed at different temperatures; Table 1 shows that with increased temperature and annealing time, the (200) peak FWHM decreases, corresponding to increasing average grain size.

Iron pyrite films that were (1) as-synthesized, (2) hydrazine treated, and (3) hydrazine treated and annealed, were used for the fabrication of Schottky junction and ZnO/FeS<sub>2</sub> or CdS/FeS<sub>2</sub> heterojunction solar cells employing FeS<sub>2</sub> NC film as the absorber layer. In all cases, results showed no improvement in PV performance resulting from hydrazine or thermal annealing treatments. PV devices yielded effectively zero photo-conversion efficiency, showing diode behavior but no open circuit voltage or short circuit current.

Kirkeminde *et al.*<sup>10</sup> prepared all inorganic iron pyrite nano-heterojunction solar cells. A blended mixture of FeS<sub>2</sub> NCs with CdS quantum dots was prepared in organic solvent to serve as the absorber layer on the ITO/PEDOT:PSS/TFB materials stack. Devices based on this FeS<sub>2</sub>:CdS bulk heterojunction absorber yielded a  $V_{OC}$  of 0.79 V,  $J_{SC}$  of 3.9 mA cm<sup>-2</sup>, FF of 36% and PCE of 1.1% under simulated AM 1.5G illumination. Similarly, Richardson *et al.*<sup>15</sup> prepared inverted bulk heterojunction solar cells using ZnO as window layer, and based on an absorber layer of 0–4 wt% FeS<sub>2</sub> NCs in P3HT:PCBM. They found that the inclusion of NC FeS<sub>2</sub> improved device performance over the P3HT:PCBM standard device, achieving 2.9% efficiency with NC FeS<sub>2</sub> vs. 2.4% without FeS<sub>2</sub>.

Since we used sputtered CdS or ZnO films as window layers and a pure FeS<sub>2</sub> NC film as absorber layer in preparing heterojunction solar cells, our method differs from those used in making the devices described in the previous paragraph. Since CdS and P3HT are both photoactive materials, one cannot easily discern the precise role played by the FeS<sub>2</sub> NCs in the above examples.

Electronic properties of FeS<sub>2</sub> NC films were studied using hot probe measurement,<sup>53</sup> four point probe measurement, and Hall measurement methods, with results summarized in Tables 2 and 3. All hot probe measurements indicated clearly that the films were p-type, in agreement with reports from other polycrystalline and NC-based films,<sup>7,10,54</sup> and indicating that the majority of charge carriers in our pyrite films are holes.

Table 2 shows the sheet resistance for two pairs of FeS<sub>2</sub> NCs on soda-lime glass, in three and four different conditions. For the first sample type, FeS<sub>2</sub> NCs were synthesized using 1,2-hexanediol/OLA and for the second case, FeS<sub>2</sub> NCs were synthesized using TOPO/OLA combinations. In the first case, three different films were prepared: the first as-synthesized NC film (No, No), the second NC film treated with hydrazine but at room temperature (Yes, No) and the third NC film treated with hydrazine and annealed in sulfur vapor for an hour at 500 °C (Yes, Yes). In the second case, one more condition, as-synthesized NC film annealed in sulfur vapor (No, Yes), is added. It is found that the films' sheet resistance decreases by a factor of ~10 when going from as-synthesized to hydrazine-treated, and by another factor of ~10 from just hydrazine-treated to hydrazine-treated and annealed. From the four point probe measurement, we see that for a sample that has been annealed but not hydrazine-treated, the sheet resistance is lower than for a sample treated with hydrazine but not annealed, and higher than for the sample which was hydrazine treated and annealed. Resistivity of the films in each case is obtained by multiplying sheet resistance by the average thickness of the films. These sheet resistance values are very close to those obtained from Hall measurement as given in Table 3. The decrease in sheet resistance of the hydrazine treated films correlates with the removal of the organic molecules from the surface of the NCs which insulate neighboring NCs against electrical conduction. When the films are annealed at high temperature, any residual organic molecules are evaporated; in addition, the increased NC grain size reduces the density of grain boundaries within the film by a factor of ~2.

Table 1 Effect of annealing temperature and time on the FWHM of the (200) XRD peak measured for FeS<sub>2</sub> NC films

Hydrazine treatment	Temperature (°C), time (hour)	$2\theta$ (°)	FWHM (mrad)	Grain size (nm)
No	Room temp	33.02	7.7	18.6
Yes	Room temp	33.02	7.9	18.0
Yes	500, 1	33.03	6.9	20.6
Yes	500, 3	33.04	6.8	21.2
No	500, 3	33.04	6.9	20.6
Yes	540, 1	33.03	6.3	22.8
Yes	540, 3	33.03	6.1	23.4

Table 2 Four point probe measurements: average thickness of the film = 3.5  $\mu\text{m}$ 

Synthesis of FeS <sub>2</sub>	Conditions		4-point probe measurement	
	Surfactant/solvent	Hydrazine treatment	Heat treatment	Sheet resistance ( $\Omega \square^{-1}$ )
1,2-Hexanediol/OLA	No	No	$3.4 \times 10^5$	119
	Yes	No	$3.5 \times 10^4$	12.2
	Yes	Yes	$6.3 \times 10^3$	2.2
TOPO/OLA	No	No	$3.8 \times 10^5$	133
	No	Yes	$7.4 \times 10^3$	2.6
	Yes	No	$3.4 \times 10^4$	11.9
	Yes	Yes	$1.5 \times 10^3$	0.52

Free carrier concentrations of the NC films increase by a factor of  $\sim 2$  following hydrazine treatment, and by another factor of  $\sim 2$  to  $\sim 5$  following sulfur annealing. The maximum carrier concentrations of treated and annealed films were of the order of  $10^{19} \text{cm}^{-3}$  or higher in some cases. Significant studies in the electrical properties of iron pyrite NC thin films based on syntheses similar to that of Bi *et al.*<sup>7</sup> and the method described here cannot be found, though related studies were reported for bulk pyrite thin film<sup>55</sup> and iron pyrite nanowires.<sup>56</sup> Carrier concentrations obtained by Huang *et al.*<sup>55</sup> for bulk FeS<sub>2</sub> thin films are reported as  $\sim 10^{18} \text{cm}^{-3}$  and carrier concentration obtained by Cabán-Acevedo *et al.*<sup>56</sup> for iron pyrite nanowires are of the order of  $10^{21} \text{cm}^{-3}$ , bracketing the values we obtained from annealed films. We find that even for our apparently pure-phase FeS<sub>2</sub> NCs, the resulting thin films possess very high carrier concentrations, and that when annealed at high temperature ( $>500 \text{ }^\circ\text{C}$ ), carrier concentrations increase. As obtained by Hall measurement, in all different conditions, the mobility of the carriers in the NC film is found to be  $\ll 1 \text{cm}^2 \text{V}^{-1} \text{s}^{-1}$ . Very low mobility strongly affects the workings of solar cells due to poor transport; in addition, high carrier concentration leads to very short or negligible depletion widths, and one would have to rely on relatively long diffusion lengths.

The built-in electric field in the depletion region of a heterojunction solar cell serves to separate the photogenerated charge carriers across the interface. If the carrier concentration in the p-region is significantly higher than for the n-region, the majority of the depletion region occurs within the n-type material. We estimate that an iron pyrite NC film with a doping

density of  $p \sim 1 \times 10^{19} \text{cm}^{-3}$  will exhibit an essentially negligible depletion width of  $<15 \text{ nm}$ ; clearly such a device would necessarily rely on diffusion-based transport. Solar cells that rely principally on diffusion transport also exhibit low trap state density and long minority carrier lifetimes, neither of which are evident within our FeS<sub>2</sub> NC-based films. Therefore, we believe that the e-h pairs photogenerated within the FeS<sub>2</sub> primarily recombine prior to diffusing to the (small) depletion region where they could be separated.

At very high free hole concentrations, the Fermi level moves into the valence band and the semiconductor layer begins to show conductivity consistent with metallic conduction. Characterizing the temperature-dependent resistivity enables investigation of degeneracy and of the dominant transport mechanisms. Fig. 4 shows the results of the temperature dependent resistivity measurements of the FeS<sub>2</sub> NC films of thickness 486 nm and 850 nm respectively in the temperature range of 80 K to 300 K. The films showed characteristic semi-conducting behavior wherein the resistivity decreased with increasing temperature – *i.e.*, the FeS<sub>2</sub> NC films have a negative temperature coefficient of resistivity over the range of 80 to 300 K. This is as-expected for a semiconducting film because the number of ionized defect states (and the concentration of free carriers) increases strongly with temperature. It can also be seen that the resistivity depends on the thickness of the film, with the thicker film showing a lower resistance.

Carrier concentration exceeding  $10^{19} \text{cm}^{-3}$  indicates near-degenerate doping. Typically, degenerately-doped semiconductor films show conductivity that is nearly independent of

Table 3 Hall measurements; average thickness of the films  $\approx 3.5 \mu\text{m}$ 

Synthesis	Conditions		Hall measurements				
	Surfactant/solvent	Hydrazine treatment	Heat treatment	Sheet resistance ( $\Omega \square^{-1}$ )	Carrier conc. ( $\text{cm}^{-3}$ )	Resistivity ( $\Omega \text{cm}$ )	Mobility ( $\text{cm}^2 \text{V}^{-1} \text{s}^{-1}$ )
TOPO/OLA	No	Room temp		$1.1 \times 10^5$	$4.3 \times 10^{18}$	139	0.04
	Yes	Room temp		$3.8 \times 10^4$	$9.7 \times 10^{18}$	13.3	0.22
	Yes	500 $^\circ\text{C}$ , 1 h		$4.3 \times 10^3$	$1.5 \times 10^{19}$	1.5	0.32
	Yes	500 $^\circ\text{C}$ , 3 h		$1.8 \times 10^3$	$3.5 \times 10^{19}$	0.6	0.37
	No	500 $^\circ\text{C}$ , 3 h		$4.9 \times 10^3$	$1.6 \times 10^{19}$	1.7	0.22
	Yes	540 $^\circ\text{C}$ , 1 h		$3.0 \times 10^3$	$3.4 \times 10^{19}$	1.1	0.17
	Yes	540 $^\circ\text{C}$ , 3 h		$1.8 \times 10^3$	$5.7 \times 10^{20}$	0.6	0.42

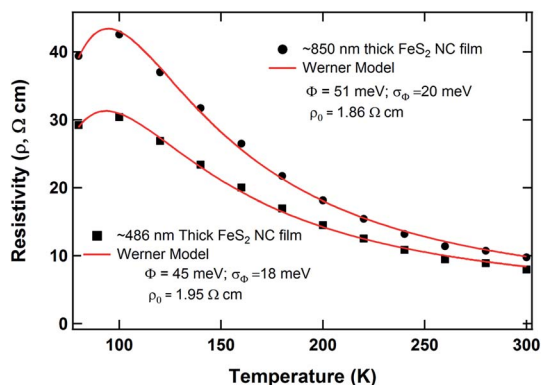


Fig. 4 Temperature dependent resistivity of the hydrazine-treated FeS<sub>2</sub> NC film of thickness ~486 nm and 850 nm prepared on soda lime glass.

temperature. In our case, a temperature-dependent conductivity indicates that a significant role is played by the high density of grain boundaries. The classical grain boundary model, as first introduced by Seto,<sup>57</sup> omits accounting for the inherent variability in potential barrier height at the grain boundaries. Werner showed that a distribution of barrier heights results in a curved Arrhenius plot of conductivity vs. temperature.<sup>58</sup> Indeed, we do observe such a temperature dependence, and find as did Seefeld *et al.*<sup>29</sup> that the NC FeS<sub>2</sub> films behave according to the Werner model based on a Gaussian distribution of barrier heights as follows:<sup>58</sup>

$$P(\Phi) = \frac{1}{\sigma_{\Phi} \sqrt{2\pi}} \exp\left(-\frac{(\bar{\Phi} - \Phi)^2}{2\sigma_{\Phi}^2}\right) \quad (1)$$

where  $\bar{\Phi}$  is the mean barrier height and  $\sigma$  is the standard deviation. According to the Werner model, the transport of carriers in polycrystalline films is limited by thermionic emission across inhomogeneous grain boundaries. In this case, the temperature dependent resistivity is given by

$$\rho = \rho_0 \exp\left[q\left(\frac{\Phi}{kT} - \frac{q\sigma_{\Phi}^2}{2k^2T^2}\right)\right] \quad (2)$$

Our temperature dependent resistivity data for two different thicknesses were fitted with this model (Fig. 4) yielding barrier height  $\Phi = 45 \pm 18$  meV for the FeS<sub>2</sub> film of thickness 486 nm and  $\Phi = 51 \pm 20$  meV for the FeS<sub>2</sub> film of thickness 850 nm respectively. From this analysis, we see that there is a good agreement between the Werner theory and the experimental results in the temperature range of 300 K to 80 K. Due to the inhomogeneity of the films, the standard deviation is relatively large.<sup>59</sup> The barrier height obtained in this work is similar to that of the nanocrystalline FeS<sub>2</sub> film obtained by Seefeld *et al.*<sup>29</sup> and smaller than that of the bulk polycrystalline film studied by Ares *et al.*<sup>60</sup> In the Seefeld *et al.* study, pyrite films were prepared from the solution phase deposition of an iron(III) acetylacetonate ink and the temperature dependent study was performed in the temperature range of 80–350 K. In Ares *et al.* study, pyrite films were prepared by thermal evaporation of iron powder on soda

lime glasses at room temperature and the temperature dependent study was performed at higher than room temperature.

Recognizing the importance of the work function to numerous electronic and optoelectronic applications, we have conducted initial UPS measurements of FeS<sub>2</sub> NC films before and after the hydrazine treatment. Details of the sample preparation and measurement methods are included in the supplementary information file. Our findings indicate work function values of 3.3 eV and 3.5 eV, respectively, for the as-synthesized FeS<sub>2</sub> NC film and for the hydrazine-treated FeS<sub>2</sub> NC film. Our search for literature reports of the work function for iron pyrite has revealed few sources for this information. In particular, Tributsch *et al.* reported a work function value of 5.0 eV,<sup>6</sup> and Trigwell *et al.* reported a work function of 5.45 eV.<sup>62</sup> Our preliminary work function results are unexpected based on the film's performance as the back contact layer to CdTe devices.<sup>61</sup> Results from additional studies of the optoelectronic behavior of hydrazine-treated FeS<sub>2</sub> NC films at the back contact of CdS/CdTe solar cells will be reported in a separate publication.

## 4. Conclusions

Iron pyrite NCs were synthesized using hot injection method in an inert atmosphere. Phase pure and highly crystalline FeS<sub>2</sub> NCs were identified using iron(II) bromide (FeBr<sub>2</sub>) as the iron precursor coordinating with TOPO or 1,2-hexanediol. From the detailed study of their electrical properties, FeS<sub>2</sub> NC-based films were found to show p-type behavior with very high carrier concentration of  $\sim 1 \times 10^{19} \text{ cm}^{-3}$ , and very low mobility of  $< 1 \text{ cm}^2 \text{ V}^{-1} \text{ s}^{-1}$ . While the high free carrier density and low mobility limit the application of these FeS<sub>2</sub> NC-based films as the absorber layer in thin film photovoltaic cells, their high conductivity and previously-reported high work function represent the material as a promising contact or buffer layer.<sup>61</sup> Temperature dependent conductivity studies revealed that despite their high carrier concentration, these FeS<sub>2</sub> NC films behave as non-degenerate semiconductors. In addition, the temperature dependent conductivity study indicated that the conductivity depends mainly on the density of grain boundaries and follows the Werner model.<sup>58</sup>

## Acknowledgements

KPB, and RJE were supported by the National Science Foundation's Sustainable Energy Pathways Program under grant CHE-1230246; KPB, PJR, TK, and RJE also gratefully acknowledge support from Air Force Research Laboratory under contracts FA9453-08-C-0172 and FA9453-11-C-0253. HC and SJ were supported by the Global Frontier R&D Program through the Center for Multiscale Energy Systems and the global R&D program. The authors thank Riza Kaya for helpful discussions, and Zhaoning Song for assistance with the sintering apparatus.

## References

- 1 P. P. Altermatt, T. Kiesewetter, K. Ellmer and H. Tributsch, *Sol. Energy Mater. Sol. Cells*, 2002, **71**, 181–195.
- 2 C. Wadia, Y. Wu, S. Gul, S. K. Volkman, J. Guo and A. P. Alivisatos, *Chem. Mater.*, 2009, **21**, 2568–2570.
- 3 L. Yu, S. Lany, R. Kykyneshi, V. Jieratum, R. Ravichandran, B. Pelatt, E. Altschul, H. A. S. Platt, J. F. Wager, D. A. Keszler and A. Zunger, *Adv. Energy Mater.*, 2011, **1**, 748–753.
- 4 K. Ellmer and C. Höpfner, *Philos. Mag. A*, 1997, **75**, 1129–1151.
- 5 A. Ennaoui and H. Tributsch, *Sol. Cells*, 1984, **13**, 197–200.
- 6 A. Ennaoui, S. Fiechter, C. Pettenkofer, N. Alonso-Vante, K. Büker, M. Bronold, C. Höpfner and H. Tributsch, *Sol. Energy Mater. Sol. Cells*, 1993, **29**, 289–370.
- 7 Y. Bi, Y. Yuan, C. L. Exstrom, S. A. Darveau and J. Huang, *Nano Lett.*, 2011, **11**, 4953–4957.
- 8 J. Puthussery, S. Seefeld, N. Berry, M. Gibbs and M. Law, *J. Am. Chem. Soc.*, 2010, **133**, 716–719.
- 9 P. S. Vasekar and T. P. Dhakal, *Sol. Cells: Res. Appl. Perspect.*, 2013, DOI: 10.5772/51734.
- 10 A. Kirkeminde, R. Scott and S. Ren, *Nanoscale*, 2012, **4**, 7649–7654.
- 11 Y.-Y. Lin, D.-Y. Wang, H.-C. Yen, H.-L. Chen, C.-C. Chen, C.-M. Chen, C.-Y. Tang and C.-W. Chen, *Nanotechnology*, 2009, **20**, 405207.
- 12 C. Lin, D. Wang, Y. Wang, C.-C. Chen, Y. Yang and Y. Chen, *Sol. Energy Mater. Sol. Cells*, 2011, **95**, 1107–1110.
- 13 D. Y. Wang, Y. T. Jiang, C. C. Lin, S. S. Li, Y. T. Wang, C. C. Chen and C. W. Chen, *Adv. Mater.*, 2012, **24**, 3415–3420.
- 14 C. Steinhagen, T. B. Harvey, C. J. Stolle, J. Harris and B. A. Korgel, *J. Phys. Chem. Lett.*, 2012, **3**, 2352–2356.
- 15 B. J. Richardson, L. Zhu and Q. Yu, *Sol. Energy Mater. Sol. Cells*, 2013, **116**, 252–261.
- 16 H. A. Macpherson and C. R. Stoldt, *ACS Nano*, 2012, **6**, 8940–8949.
- 17 J. M. Lucas, C.-C. Tuan, S. D. Lounis, D. K. Britt, R. Qiao, W. Yang, A. Lanzara and A. P. Alivisatos, *Chem. Mater.*, 2013, **25**, 1615–1620.
- 18 W. Li, M. Döblinger, A. Vaneski, A. L. Rogach, F. Jäckel and J. Feldmann, *J. Mater. Chem.*, 2011, **21**, 17946–17952.
- 19 L. Zhu, B. J. Richardson and Q. Yu, *Nanoscale*, 2014, **6**, 1029–1037.
- 20 M. Akhtar, J. Akhter, M. A. Malik, P. O'Brien, F. Tuna, J. Raftery and M. Helliwell, *J. Mater. Chem.*, 2011, **21**, 9737–9745.
- 21 D. Wang, Q. Wang and T. Wang, *CrystEngComm*, 2010, **12**, 3797–3805.
- 22 L. Zhu, B. Richardson, J. Tanumihardja and Q. Yu, *CrystEngComm*, 2012, **14**, 4188–4195.
- 23 N. G. Larsen, P. D. W. Boyd, S. J. Rodgers, G. E. Wuenschell, C. A. Koch, S. Rasmussen, J. R. Tate, B. S. Erler and C. A. Reed, *J. Am. Chem. Soc.*, 1986, **108**, 6950–6960.
- 24 J. P. Collman, R. R. Gagne, C. Reed, T. R. Halbert, G. Lang and W. T. Robinson, *J. Am. Chem. Soc.*, 1975, **97**, 1427–1439.
- 25 J. J. Choi, J. Luria, B.-R. Hyun, A. C. Bartnik, L. Sun, Y.-F. Lim, J. A. Marohn, F. W. Wise and T. Hanrath, *Nano Lett.*, 2010, **10**, 1805–1811.
- 26 A. Yamamoto, M. Nakamura, A. Seki, E. L. Li, A. Hashimoto and S. Nakamura, *Sol. Energy Mater. Sol. Cells*, 2003, **75**, 451–456.
- 27 Y. Z. Dong, Y. F. Zheng, H. Duan, Y. F. Sun and Y. H. Chen, *Mater. Lett.*, 2005, **59**, 2398–2402.
- 28 L. Huang, F. Wang, Z. Luan and L. Meng, *Mater. Lett.*, 2010, **64**, 2612–2615.
- 29 S. Seefeld, M. Limpinsel, Y. Liu, N. Farhi, A. Weber, Y. Zhang, N. Berry, Y. J. Kwon, C. L. Perkins, J. C. Hemminger, R. Wu and M. Law, *J. Am. Chem. Soc.*, 2013, **135**, 4412–4424.
- 30 J. M. Luther, M. Law, M. C. Beard, Q. Song, M. O. Reese, R. J. Ellingson and A. J. Nozik, *Nano Lett.*, 2008, **8**, 3488–3492.
- 31 J. Tang, X. Wang, L. Brzozowski, D. A. R. Barkhouse, R. Debnath, L. Levina and E. H. Sargent, *Adv. Mater.*, 2010, **22**, 1398–1402.
- 32 M. Birkholz, S. Fiechter, A. Hartmann and H. Tributsch, *Phys. Rev. B: Condens. Matter Mater. Phys.*, 1991, **43**, 11926–11936.
- 33 G. Smestad, A. Ennaoui, S. Fiechter, H. Tributsch, W. K. Hofmann, M. Birkholz and W. Kautek, *Sol. Energy Mater.*, 1990, **20**, 149–165.
- 34 I. J. Ferrer, D. M. Nevskaja, C. de las Heras and C. Sánchez, *Solid State Commun.*, 1990, **74**, 913–916.
- 35 N. M. Ravindra and V. K. Sritastava, *Phys. Status Solidi A*, 1981, **65**, 737–742.
- 36 C. de las Heras and G. Lifante, *J. Appl. Phys.*, 1997, **82**, 5132.
- 37 C. de las Heras, I. J. Ferrer and C. Sanchez, *J. Phys.: Condens. Matter*, 1994, **6**, 10177.
- 38 A. M. Karguppikar and A. G. Vedeshwar, *Phys. Status Solidi A*, 1988, **109**, 549–558.
- 39 W. W. Kou and M. S. Seehra, *Phys. Rev. B: Condens. Matter Mater. Phys.*, 1978, **18**, 7062–7068.
- 40 D. A. R. Barkhouse, O. Gunawan, T. Gokmen, T. K. Todorov and D. B. Mitzi, *Progress in Photovoltaics: Research and Applications*, 2012, **20**, 6–11.
- 41 T. K. Todorov, J. Tang, S. Bag, O. Gunawan, T. Gokmen, Y. Zhu and D. B. Mitzi, *Adv. Energy Mater.*, 2013, **3**, 34–38.
- 42 S. N. White, *Chem. Geol.*, 2009, **259**, 240–252.
- 43 A. Kleppe and A. Jephcoat, *Mineral. Mag.*, 2004, **68**, 433–441.
- 44 M. Eghbalnia, PhD Doctor of Philosophy dissertation, University of British Columbia, 2012.
- 45 A. Boughriet, R. S. Figueiredo, J. Laureyns and P. Recourt, *J. Chem. Soc., Faraday Trans.*, 1997, **93**, 3209–3215.
- 46 C. Rémazeilles, M. Saheb, D. Neff, E. Guilminot, K. Tran, J.-A. Bourdoiseau, R. Sabot, M. Jeannin, H. Matthiesen, P. Dillmann and P. Refait, *J. Raman Spectrosc.*, 2010, **41**, 1425–1433.
- 47 N. Gupta, G. F. Alapatt, R. Podila, R. Singh and K. F. Poole, *Int. J. Photoenergy*, 2009, 2009.
- 48 M. Gong, A. Kirkeminde and S. Ren, *Sci. Rep.*, 2013, **3**, 2092.
- 49 N. Alonso-Vante, G. Chatzitheodorou, S. Fiechter, N. Mgoduka, I. Poullos and H. Tributsch, *Sol. Energy Mater.*, 1988, **18**, 9–21.



- 50 S. Fiechter, M. Birkholz, A. Hartmann, P. Dulski, M. Giersig, H. Tributsch and R. J. D. Tilley, *J. Mater. Res.*, 1992, **7**, 1829–1838.
- 51 S. Kment, H. Kmentova, A. Sarkar, R. J. Soukup, N. J. Ianno, J. Krysa, Z. Hubicka, J. Olejnicek, C. L. Exstrom and S. A. Darveau, *Photovoltaic Specialists Conference (PVSC), 2011 37th IEEE*, 2011.
- 52 G. Smestad, A. Da Silva, H. Tributsch, S. Fiechter, M. Kunst, N. Meziani and M. Birkholz, *Sol. Energy Mater.*, 1989, **18**, 299–313.
- 53 B. G. Jung, S.-H. Min, C.-W. Kwon, S.-H. Park, K.-B. Kim and T.-S. Yoon, *J. Electrochem. Soc.*, 2009, **156**, K86–K90.
- 54 G. Golan, A. Axelevitch, B. Gorenstein and V. Manevych, *Microelectron. J.*, 2006, **37**, 910–915.
- 55 L. Y. Huang Liuyi and M. Liang, *J. Mater. Sci. Technol.*, 2009, **25**, 5.
- 56 M. Cabán-Acevedo, M. S. Faber, Y. Tan, R. J. Hamers and S. Jin, *Nano Lett.*, 2012, **12**, 1977–1982.
- 57 J. Y. W. Seto, *J. Appl. Phys.*, 1975, **46**, 5247–5254.
- 58 J. Werner, *Solid State Phenom.*, 1994, **37**, 213–218.
- 59 N. Hamdadou, A. Khelil and J. Bernede, *Mater. Chem. Phys.*, 2003, **78**, 591–601.
- 60 J. Ares, A. Pascual, I. Ferrer and C. Sanchez, *Thin Solid Films*, 2004, **451**, 233–236.
- 61 K. P. Bhandari, R. R. Khanal, N. R. Paudel, P. Koirala, P. J. Roland, T. Kinner, Y. Yanfa, R. W. Collins, M. J. Heben and R. J. Ellingson, *Photovoltaic Specialist Conference (PVSC), 2014 IEEE 40th*, Denver, CO, 2014.
- 62 S. Trigwell, M. Mazumder and R. Pellissier, *J. Vac. Sci. Technol., A*, 2001, **19**, 1454–1459.